ECO-FRIENDLY REMOVAL OF CIBACRON BLUE FROM WASTEWATER USING NANO-MODIFIED IRAQI BENTONITE: KINETICS, ISOTHERMS, AND MECHANISM

Atheer Abdulsahib ALI[1], Hamid S. METEAB[2], Amal Fadhil KAMIL[3], Hussein Fawzi HUSSEIN [4*]

This study investigates the removal of Cibacron Blue dye from aqueous solution using natural bentonite (NB) and nano-modified bentonite (NPB) as low-cost and eco-friendly adsorbents. Nano-bentonite was prepared using a reagent-free physical modification route involving washing, drying, planetary milling, hydrocyclone classification, magnetic separation, and ultrasonic delamination, without the use of any chemical reagents. Structural and surface characteristics of NB and NPB were analyzed using X-ray diffraction (XRD), Fourier transform infrared spectroscopy (FTIR), Brunauer–Emmett–Teller (BET) surface area analysis, and scanning electron microscopy (SEM), confirming particle size reduction, increased surface area, and preservation of bentonite structural integrity after nano-modification. Batch adsorption experiments were conducted to evaluate the effects of pH, contact time, adsorbent dosage, initial dye concentration, and temperature on dye removal efficiency. The results demonstrated that NPB exhibited significantly higher adsorption capacity compared to NB due to its enhanced surface activity and porosity. Adsorption behavior followed the Langmuir isotherm model and pseudo-second-order kinetic model, indicating monolayer chemisorption as the dominant mechanism. Thermodynamic analysis revealed that the adsorption process is spontaneous and endothermic. These findings highlight nano-modified bentonite as an effective and sustainable adsorbent for the removal of textile dyes from wastewater.

Keywords: Nano particles(NPs), Natural Bentonite, Cibacron blue, Adsorption

1. Introduction

Textile industries generate large volumes of colored effluents containing synthetic dyes that are discharged into the aquatic environment without adequate treatment, causing severe ecological and health problems [1–3]. These dyes are designed to resist light, temperature, and microbial degradation, which makes them persistent pollutants in surface and groundwater [4–6]. Reactive dyes, particularly those belonging to the Cibacron family, are widely used for cotton and cellulose

[1] Department of Chemistry, College of Science, Wasit University, Wasit, Iraq
[2] Scientific Research Commission, Baghdad, Iraq
[3] Ministry of Education, Directorate of Wasit Education, Wasit, Iraq
[4] * PhD Eng., Scientific Research Commission, Baghdad, Iraq, Corresponding author: e-mail hussein.f.hussein@src.edu.iq

fabrics because of their high fixation efficiency and bright shades; however, they exhibit low biodegradability and can hinder sunlight penetration and photosynthesis in aquatic systems [7–9].

Various physicochemical and biological methods—such as coagulation–flocculation, advanced oxidation, membrane filtration, and microbial degradation—have been proposed for dye removal [10–12]. Nevertheless, many of these methods suffer from drawbacks such as high operational cost, incomplete color removal, generation of secondary sludge, or requirement for sophisticated facilities [13]. Among the available alternatives, adsorption has attracted increasing attention due to its operational simplicity, flexibility, and high efficiency even at low pollutant concentrations [14, 15]. The performance of the adsorption process depends strongly on the surface characteristics, porosity, and chemical activity of the adsorbent material [16].

Natural clays are inexpensive, abundant, and environmentally benign materials that have demonstrated excellent potential as adsorbents for organic dyes and heavy metals [17, 18]. Bentonite, a montmorillonite-rich aluminosilicate, is particularly interesting because of its layered structure, high cation-exchange capacity, and large specific surface area [19]. Its adsorption performance can be further improved through activation, ion exchange, or size-reduction treatments that increase the number of accessible active sites [20, 21]. The transformation of bulk bentonite into nano-bentonite via mechanical or ultrasonic milling has been shown to enhance surface reactivity and shorten intraparticle diffusion pathways.

Several studies have explored the application of modified clays for the removal of reactive dyes. However, most of these studies involve chemical reagents that increase processing costs and may generate additional waste. In contrast, mechanical Nano sizing offers a eco-friendlier and more scalable route to improving bentonite performance without introducing foreign chemicals. This strategy aligns with sustainable development principles aimed at minimizing secondary pollution and energy consumption [22, 23, 24].

Accordingly, the present study focuses on the eco-friendly preparation of nano-bentonite using mechanical milling and ultrasonic treatment, and its application for the removal of Cibacron Blue dye from aqueous solution. The objectives are to (i) characterize the structural and morphological features of both natural and nano-bentonite using FTIR, XRD, SEM, EDX, and BET techniques; (ii) evaluate the effects of key parameters such as pH, contact time, adsorbent dose, and initial dye concentration; and (iii) model the adsorption behavior through kinetic, isotherm, and thermodynamic analyses to elucidate the mechanism of dye uptake. The findings are expected to contribute to the development of low-cost and environmentally sustainable adsorbents for wastewater purification in textile and related industries.

2. Experimental work

Raw bentonite clay from local Iraqi deposits was washed repeatedly with distilled water to remove soluble salts and organic contaminants, oven-dried at 100 °C (24 h), and preliminarily milled to reduce coarse fractions. Mechanical size reduction was performed using a PM-400 planetary mill operated at 200 rpm for 10 h to obtain a fine powder; the milled material was then purged of ferrous and titanium impurities by magnetic separation (GYH3) and processed through a 2″ VorSpin hydrocyclone (AZ model) to remove free silica and light particulates. The cleaned slurry was subjected to ultrasonic dispersion (UP200S) for 2 h to promote exfoliation and obtain a nanoscale fraction, which after drying at 100 °C served as the nano-bentonite adsorbent [9]. Cibacron Blue P-3R (analytical grade) was used to prepare a 1000 mg•L^{-1} stock solution and working solutions (10–100 mg•L^{-1}) by serial dilution; calibration curves (absorbance vs concentration) were constructed with a UV–Vis spectrophotometer (Shimadzu UV-1800) at the dye maximum wavelength (λmax ≈ 605 nm) for quantitative determinations [22–24]. Structural and surface characterization of bulk and nano samples employed FTIR (Shimadzu 8400S, 4000–400 cm^{-1}), XRD (Shimadzu 6000, Cu-Kα, 2θ range 5–80°), SEM-EDX (TESCAN MIRA3), AFM (Integra), and N_2 adsorption–desorption (BET, HORIBA SA-9600) following standard laboratory procedures [25, 26]. Batch adsorption tests were conducted in 250 mL conical flasks containing 50 mL dye solution and a measured mass of adsorbent; suspensions were agitated at 200 rpm in a thermostatic orbital shaker while varying pH (2–10, adjusted with 0.1 M HCl or 0.1 M NaOH), adsorbent dose (0.05–0.30 g), initial dye concentration (10–100 mg•L^{-1}) and temperature (25–45 °C). After equilibration the suspensions were filtered and the residual dye concentration was read spectrophotometrically, the equilibrium adsorption capacity Qe calculated by the mass-balance relation.

$$Q_e = \frac{(C_0\text{-}C_e) \times V}{M} \quad (1$$

Where; Q_e : equilibrium adsorption capacity (mg·g^{-1}), C_0 : initial dye concentration in solution (mg·L^{-1}) and Ce : equilibrium dye concentration in solution (mg·L^{-1}), V: volume of dye solution (L), M: mass of adsorbent used (g), This equation determines the amount of dye adsorbed per unit mass of adsorbent at equilibrium.

Kinetic data were analyzed using pseudo-first-order and pseudo-second-order models, and equilibrium data were fitted to Langmuir and Freundlich isotherms using non-linear regression to obtain model parameters and goodness-of-fit metrics. Thermodynamic quantities (ΔG°, ΔH°, ΔS°) were derived from temperature-dependent equilibrium constants via the Van't Hoff relation to assess

spontaneity and the endothermic/exothermic nature of adsorption. All experiments were performed in duplicate and representative data are reported as mean values.

3. Results and discussion

A. FTIR

FTIR spectroscopy was employed to identify the characteristic functional groups of both natural and nano-sized bentonite (Fig. 1). The spectra of bulk bentonite displayed strong absorption bands near 3620 cm^{-1} and 3420 cm^{-1}, corresponding to structural –OH stretching and interlayer water vibrations, respectively. The band around 1635 cm^{-1} represents H–O–H bending of adsorbed water molecules. Peaks at 1115 cm^{-1} and 1005 cm^{-1} are associated with Si–O–Si stretching, whereas those at 915 cm^{-1} and 792 cm^{-1} indicate Al–Al–OH and Fe–Mg–OH vibrations. The nano-bentonite exhibited slight shifts and reduced band intensity, implying partial delamination and exposure of new reactive sites after mechanical milling and ultrasonic treatment. These spectral modifications confirm successful structural alteration and formation of nano-bentonite.

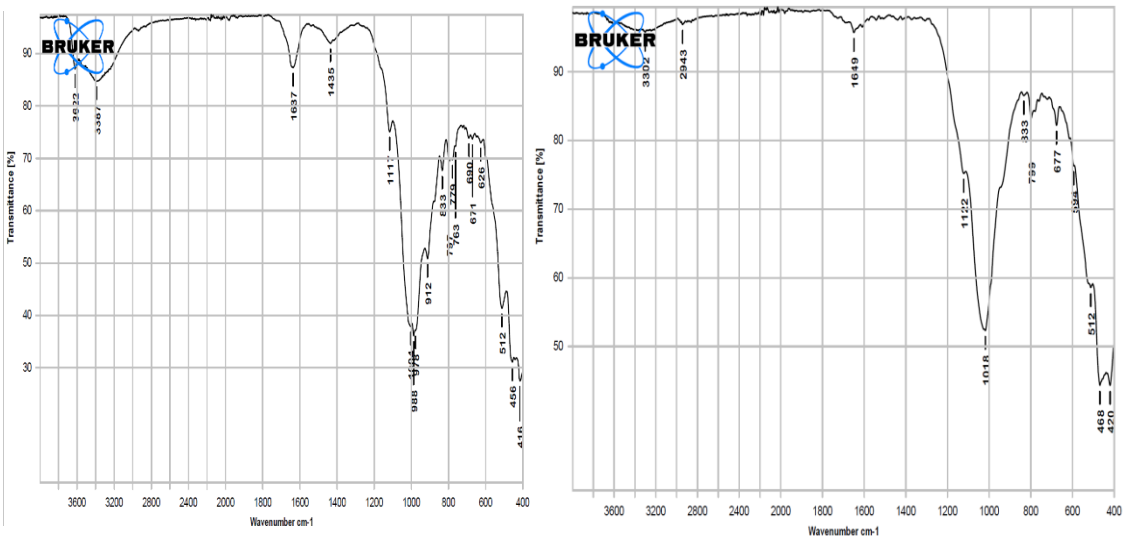

A B

Fig. 1. (A) FTIR of Bentonite, (B) FTIR of Nano Bentonite

B. X-ray diffraction

The X-ray diffraction patterns (Fig. 2) show the characteristic reflections of montmorillonite and minor quartz impurities. The main basal spacing (d001) of natural bentonite appeared at $2\theta \approx 6.3°$, corresponding to an interlayer spacing of

14.0 Å. After nano-sizing, this reflection broadened and slightly shifted to higher 2θ, indicating partial layer disorder and reduction of crystal size. The diminished peak intensities at 19.8°, 27.1°, and 35.0° further suggest structural distortion due to mechanical milling. These variations confirm the transformation of crystalline bentonite into a less ordered nanostructure without phase decomposition [27].

$$R\% = \frac{(C_0 - C_t)}{C_0} \times 100 \qquad (2)$$

Where R%: dye removal efficiency (%), C_0: initial concentration of dye ($mg \cdot L^{-1}$), C_t: dye concentration at time t ($mg \cdot L^{-1}$), t: contact time (min), this equation expresses the percentage of dye removed from solution at any given time.

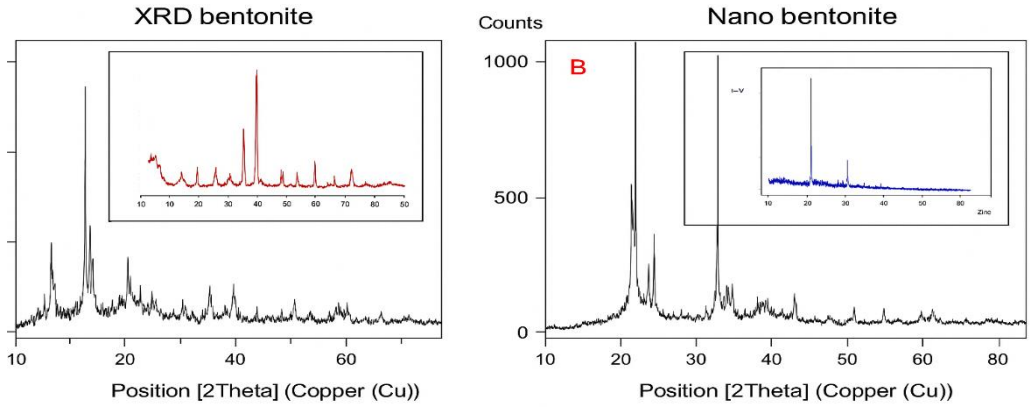

A B

Fig. 2. (A) XRD of Bentonite, (B) XRD of Nano Bentonite

C. Surface area

The surface area of natural and nano-bentonite was determined to be 35 and 173 m^2/g, respectively. The remarkable increase in surface area after nanosizing is mainly attributed to structural deformation and the removal of interlayer cations, which led to a more open and accessible structure. These structural modifications were confirmed through Atomic Force Microscopy (AFM), Scanning Electron Microscopy (SEM), and surface area analyses (BET and BJH methods). AFM results revealed that the average particle diameter of the nano-bentonite was approximately 50 nm, with a particle-size distribution ranging from 10 to 100 nm, as shown in Fig. 3(a). The three-dimensional surface morphology presented in Fig. 3(b) demonstrates a uniform and finely dispersed structure with reduced surface irregularities. The measured root mean square roughness (Ra) value of 15.58 nm indicates the material's Nano scale uniformity and confirms the absence of large

particle agglomerations. This observation provides clear evidence of the homogeneity and high degree of dispersion achieved through mechanical milling and ultrasonic treatment [23].

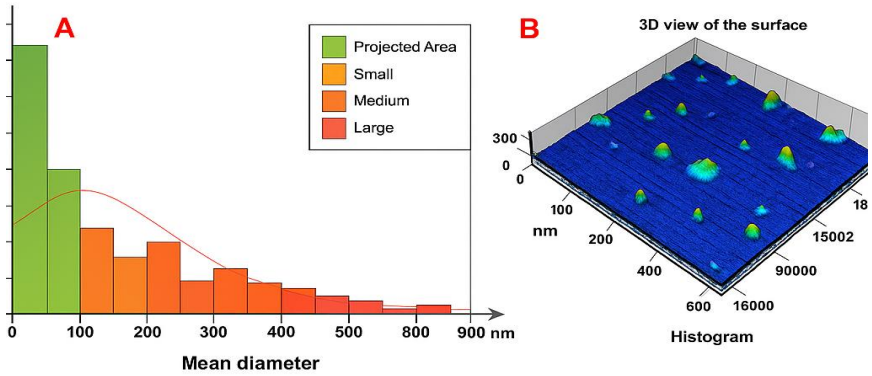

A B

Fig. 3. (A) The particle size distribution, (B) Morphology of Nano Bentonite.

The SEM micrograph shown in Fig. 4 illustrates the surface morphology of the prepared nano-bentonite particles. The image reveals semi-spherical aggregates with relatively uniform size distribution, confirming the successful formation of homogeneous nanoparticles. These nano-particles appear as crystalline domains with minimal aggregation, averaging 45.89 nm in size, which agrees well with the crystallite dimensions estimated from XRD analysis.

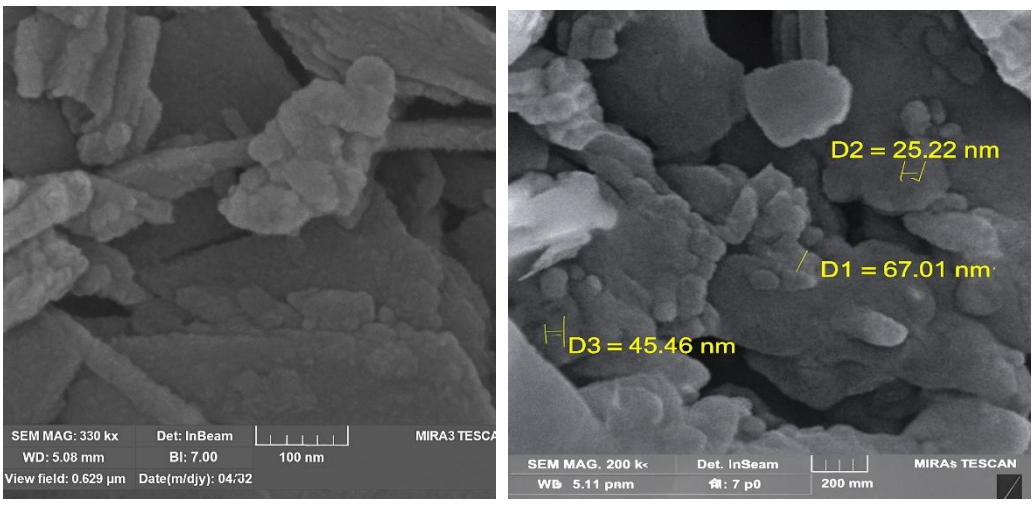

Fig. 4. SEM micrographs of bentonite: (A) bulk bentonite showing stacked lamellae and irregular aggregates; (B) nano-bentonite revealing uniformly dispersed semi-spherical particles with minimal agglomeration (average size ≈ 45–50 nm).

Energy-dispersive X-ray (EDX) analysis, presented in Fig. 5, was employed to identify the elemental composition of the nano-bentonite. The spectrum exhibited distinct peaks corresponding to carbon (C), oxygen (O), silicon (Si), magnesium (Mg), calcium (Ca), iron (Fe), and phosphorus (P), consistent with the natural composition of bentonite minerals. The quantitative EDX data are summarized in Table 1, showing good agreement between experimentally obtained and theoretically calculated values. These results confirm that the nanosizing process did not alter the essential elemental composition of the material but only modified its structural configuration.

Table 1

Quantitative elemental composition of nano-bentonite (EDX).

No.	Element	**Wt. (%)**
1	C	28.31
2	O	38.16
3	Si	24.00
4	Mg	3.52
5	Ca	1.70
6	Fe	1.38
7	P	2.93

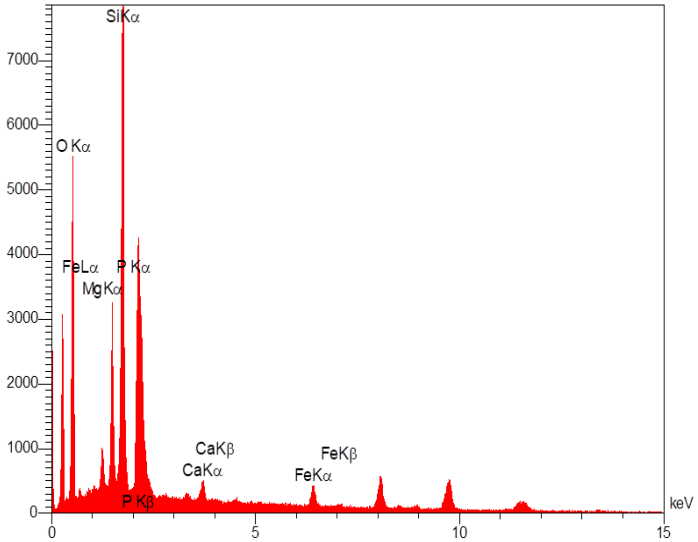

Fig. 5. Image EDX of Bentonite NPs.

Surface area and pore characteristics were determined using the Brunauer–Emmett–Teller (BET) and Barrett–Joyner–Halenda (BJH) methods. As shown in Table 2, the BET surface area of bentonite clay was 36.51 m^2/g, and the average pore diameter was 13.47 nm. The nitrogen adsorption–desorption isotherms (Fig. 6a) exhibited a Type III isotherm with an H3 hysteresis loop (Fig. 6b) according to IUPAC classification, indicating the presence of slit-shaped mesopores. The pore-size distribution confirmed a predominantly meso porous structure, with pore diameters less than 50 nm. These findings demonstrate that the applied mechanical and ultrasonic treatment increased the specific surface area while preserving the meso porous texture of the bentonite, thus enhancing its suitability for adsorption applications.

Table 2

Surface area analysis (BET, BJH) of Bentonite clay

Sample	Surface area (Single point) m^2/g	Surface area (Multiple point) m^2/g	Pore diameter (nm)	Isotherm type	Type of pore
Bentonite clay	33.79	36.51	13.47	III	Meso porous

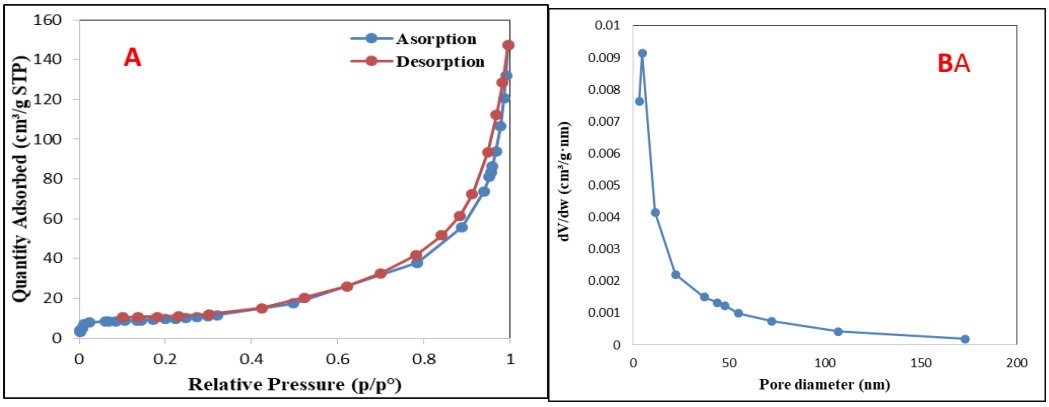

A **B**

Fig. 6. (A) Nitrogen adsorption-desorption isotherms of Bentonite clay,(B) Pore size distribution curve of Bentonite clay

D. Adsorption

The adsorption performance of the prepared bentonite and nano-bentonite was investigated to evaluate their capacity for Cibacron Blue dye removal. The calibration curve of the dye, constructed using concentrations ranging from 5 to 55 mg/L at a maximum wavelength (λ_{max}) = 605 nm, exhibited excellent linearity (R^2 = 0.9972), confirming the reliability and accuracy of the analytical measurements. The adsorption isotherms were then analyzed to interpret the interaction between the adsorbent and dye molecules, applying both Freundlich and Langmuir models. The Freundlich equation (Eq. 3) expresses the relationship between equilibrium concentration and the amount adsorbed at equilibrium.

$$\log(Q_e) = \log K_F + (\frac{1}{n})\ \log(\ C_e) \tag{3}$$

Where Q_e: equilibrium adsorption capacity ($mg \cdot g^{-1}$), C_e: equilibrium dye concentration ($mg \cdot L^{-1}$), K_F: Freundlich constant related to adsorption capacity [$(mg \cdot g^{-1})(L \cdot mg^{-1})^{1/n}$], n: Freundlich exponent related to adsorption intensity (dimensionless), the Freundlich model describes multilayer adsorption on heterogeneous surfaces.

The linear plots obtained in Fig. 7(a–b) show the fitted Freundlich isotherms for bentonite and nano-bentonite, from which the slope and intercept were used to estimate these constants

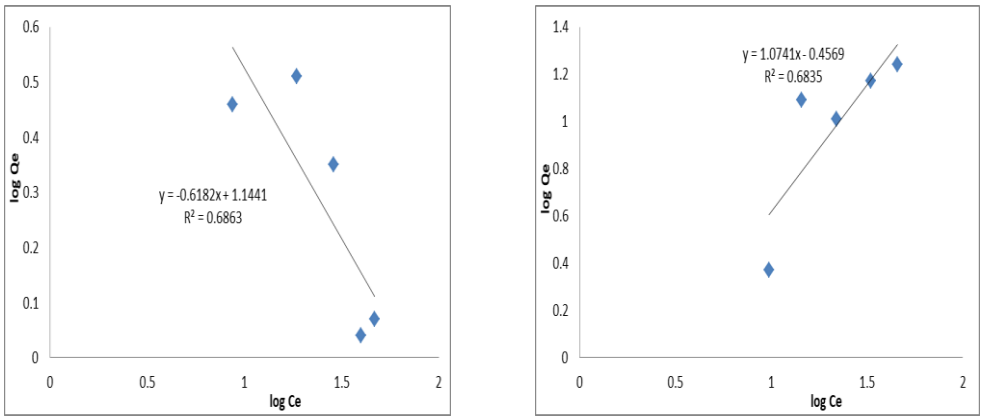

A B

Fig. 7. (A) Adsorption curves of Freundlich isotherm for Bentonite, (B) Adsorption curves of Freundlich isotherm for Bentonite NPs.

Langmuir adsorption behavior was also evaluated using Eqs. (4) and (5), which describe monolayer adsorption on a homogeneous surface.

$$\frac{C_e}{Q_e} = \frac{1}{q_{max}} K_L + \frac{C_e}{q_{max}} \quad (4)$$

$$R_L = \frac{1}{(1+K_L C_0)} \quad (5)$$

Where C_e: equilibrium concentration ($mg \cdot L^{-1}$), Q_e: amount of adsorbed dye at equilibrium ($mg \cdot g^{-1}$), q_{max}: maximum monolayer adsorption capacity ($mg \cdot g^{-1}$), K_L: Langmuir constant related to adsorption energy ($L \cdot mg^{-1}$), R_L: separation factor (dimensionless), C_0: initial dye concentration ($mg \cdot L^{-1}$), the Langmuir model assumes monolayer adsorption on a homogeneous surface. The parameters q max and Kl correspond to maximum adsorption capacity and Langmuir constant, respectively, while the separation factor Rl values ($0 < RL < 1$) indicate the favorability of the process. The results obtained in Fig. 8(a–b) demonstrate that both bentonite and nano-bentonite exhibit favorable adsorption characteristics, with the nano form showing a higher dye affinity due to its larger surface area and enhanced active sites

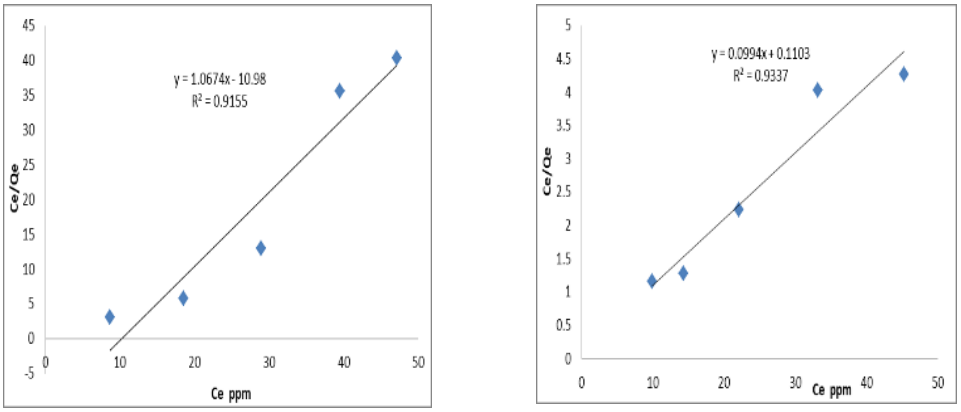

A **B**

Fig. 8. (A) Adsorption curves of Langmuir isotherm for Bentonite, (B) Adsorption curves of Langmuir isotherm for Bentonite NPs.

The effect of contact time on the adsorption process was examined by mixing 50 mL of dye solution (30 ppm) with 0.046 g of each adsorbent and agitating the mixture at 200 rpm and 298 K. As shown in Fig. 9(a–b), adsorption was initially rapid during the first few minutes owing to the large number of vacant surface sites on the nano-bentonite, followed by a gradual approach to equilibrium after approximately 75 minutes as surface saturation occurred. The stronger interaction between dye molecules and nano-bentonite indicates a higher adsorption rate

compared with bulk bentonite. These results indicate that equilibrium was achieved within 75 min, consistent with the pseudo-second-order kinetic model (see Fig. 9).

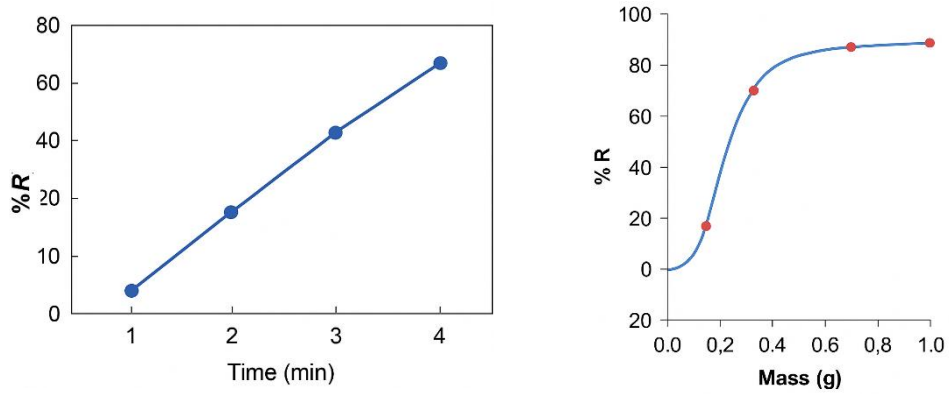

A B

Fig. 9. Effect of contact time on Cibacron Blue removal efficiency (%R) at 298 K and 200 rpm for (A) bulk bentonite and (B) nano-bentonite. Conditions: C_0 = 30 mg·L^{-1}; adsorbent dose = 0.046 g; V = 10 mL; equilibrium ~75 min.

The adsorption rate tends to stabilize beyond 0.46 g due to site overlapping (see Fig. 10), reveal that dye removal efficiency increases with adsorbent mass due to the higher number of available active sites and larger surface area, although beyond a certain dosage, the adsorption rate tends to stabilize due to overlapping of adsorption sites [28].

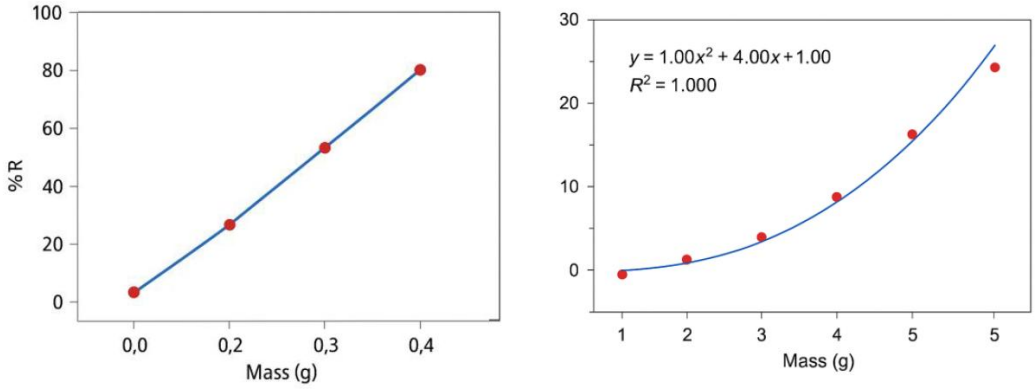

A B

Fig. 10. Effect of adsorbent mass on removal efficiency (%R) at 298 K and 200 rpm for (A) bulk bentonite and (B) nano-bentonite. Conditions: C_0 = 30 mg·L^{-1}; contact time = 75 min; V = 10 mL.

The effect of temperature and thermodynamic parameters was analyzed at 15, 25, 35, 45, and 55 °C. An increase in adsorption capacity with rising temperature indicates that the adsorption on nano-bentonite is an endothermic process, while the

process on bulk bentonite is exothermic. Thermodynamic parameters were determined using Eqs. (6)–(7), where ΔG°, ΔH°, and ΔS° represent Gibbs free energy, enthalpy, and entropy changes, respectively. The corresponding Van't Hoff plots (Fig. 11a–b) yielded ΔH° values of –58.36 kJ/mol for bulk bentonite and +2.827 kJ/mol for nano-bentonite, while ΔS° values were –2.128 and +0.002 kJ/mol•K^{-1}, respectively. The positive ΔG° for bulk (+575.784 kJ/mol) indicates non-spontaneous adsorption, whereas the negative value for nano-bentonite (–715.651 kJ/mol) confirms a spontaneous and favorable process at 298 K [29].

$$\Delta G^\circ = -RT \ln K_e \tag{6}$$

$$\ln K_e = -\frac{\Delta H^\circ}{RT} + \frac{\Delta S^\circ}{R} \tag{7}$$

Where ΔG° :standard Gibbs free energy change (kJ·mol^{-1}), ΔH°:standard enthalpy change (kJ·mol^{-1}), R: universal gas constant = 8.314 J·mol^{-1}·K^{-1}, T:absolute temperature (K), K_e : : equilibrium constant (dimensionless), these equations determine the spontaneity and thermal nature of the adsorption process.

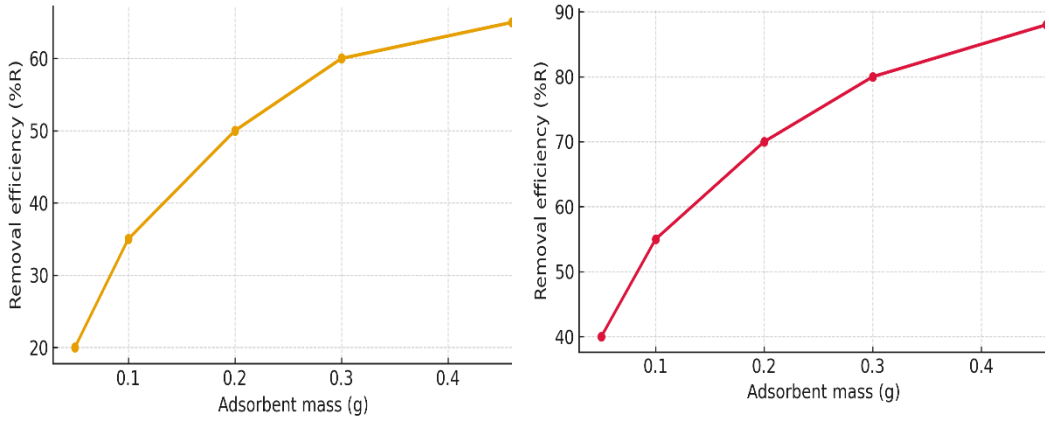

A **B**

Fig. 11. (A) Relation in (Ke) vs 1/T for the Bentonite, (B) Relation ln(Ke) vs 1/T for the Bentonite NPs.

Kinetic analysis was conducted to understand the adsorption mechanism. The equilibrium adsorption time for both adsorbents was about 75 min, as confirmed by kinetic modeling. The pseudo-first-order model, expressed by Eq. (8), and the pseudo-second-order model, expressed by Eq. (9), were both tested to describe the experimental data. The kinetic plots (Figs. 12a–b and 13a–b) demonstrate that the pseudo-second-order model fits the data better, with a higher correlation coefficient (R^2 = 0.9924 for nano-bentonite and 0.9667 for bulk

bentonite), suggesting that chemisorption involving valence-force interactions is the dominant mechanism. These results indicate that adsorption on nano-bentonite is governed by both surface and intraparticle diffusion, leading to improved performance compared with untreated bentonite.
Pseudo-first-order model:

$$\ln(q_e - q_t) = \ln q_e - K_1 t \quad (8)$$

Pseudo-second-order model:

$$\frac{t}{q_t} = \frac{1}{k_2 q_e^2} + \frac{t}{q_e} \quad (9)$$

Where q_t : amount of dye adsorbed at time t ($mg \cdot g^{-1}$), q_e : amount of dye adsorbed at equilibrium ($mg \cdot g^{-1}$), K1 : : pseudo-first-order rate constant (min^{-1}), K2 : : pseudo-second-order rate constant ($g \cdot mg^{-1} \cdot min^{-1}$), t : contact time (min), these kinetic models describe the adsorption rate and the mechanism controlling it, A better fit to the pseudo-second-order model suggests chemisorption as the dominant mechanism.

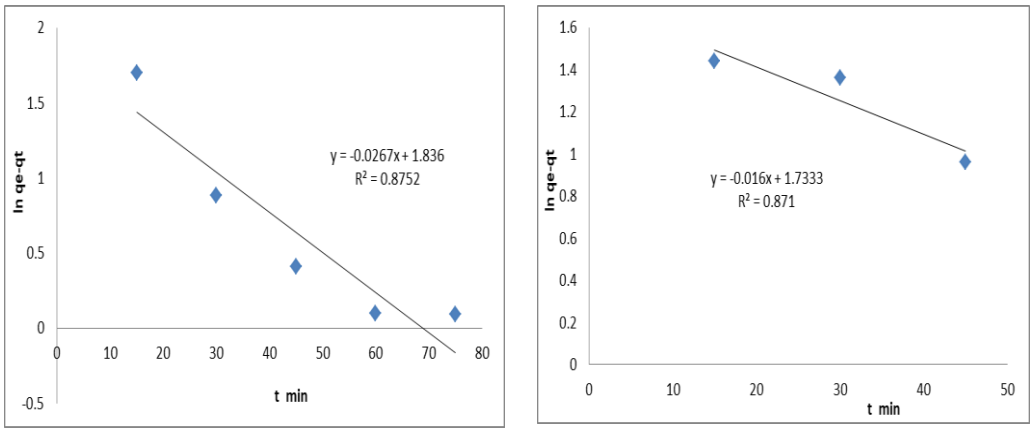

A **B**

Fig.12. (A) Curve of pseudo-first-order for Bentonite, (B) Curve of pseudo- first -order for Bentonite NPs.

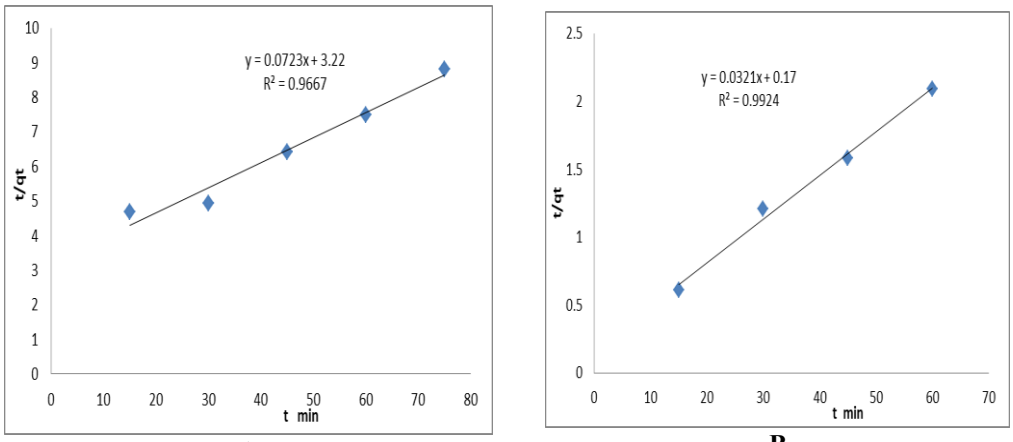

Fig.13. (A) Curve of pseudo- second -order for Bentonite, (B) Curve of pseudo-second-order for Bentonite NPs.

4. Conclusion

This study successfully demonstrated the preparation of bentonite nanoparticles from natural bentonite ore through physical treatment methods, resulting in a significant increase in surface area and enhanced physicochemical activity. The synthesized nano-bentonite exhibited excellent potential for applications in polymer nanocomposites, catalysis, and wastewater treatment. Kinetic and thermodynamic investigations confirmed that the adsorption of Cibacron Blue followed the Langmuir isotherm model, with nano-bentonite showing a higher adsorption capacity than bulk bentonite. The process was endothermic and spontaneous for the nanoparticles, while exothermic and non-spontaneous for the bulk material. Kinetic analysis revealed that the adsorption behavior is best described by the pseudo-second-order model, indicating chemisorption as the rate-controlling mechanism. Overall, the results confirm that reducing bentonite to the nanoscale considerably improves its adsorption efficiency and establishes it as a promising, eco-friendly adsorbent for dye removal and related environmental applications.

REFERENCES

[1] Aboud, N.A.A., Alkayat, W. M. S., & Hussain, D. H. (2020). Simple chemical synthesis of zinc oxide and copper oxide nanoparticles for biological protection. Systematic Reviews in Pharmacy, 11(6), 1188–1195.

[2] Aboud, N.A.A., Jasim, B.E., & Rheima, A.M. (2021). Adsorption study of phosphate ions pollution in aqueous solutions using microwave synthesized magnesium oxide nanoparticles. Journal of Physics: Conference Series, 1664(1), 801–807.

[3] Ali, A.A., Al-Hassani, R. M., & Hussain, D.H. (2020). Synthesis, spectroscopic characterization, pharmacological evaluation, and cytotoxicity assays of novel nano and

micro-scale copper (II) complexes against human breast cancer cells. International Journal of Pharmaceutical Research, 14(1), 31–39.
[4] Al-Sarray, A. J. A., Jasim, B. E., & Aboud, N. A. A. (2024). Enhancing the photostability of poly(vinyl chloride) (PVC) through the incorporation of cerium and samarium oxide. Polymer, 48(2), 188–194.
[5] Awasthi, A., Jadhao, P., & Kumari, K. (2019). Clay nano-adsorbent: Structures, applications and mechanism for water treatment. SN Applied Sciences, 1(9), 1–21. https://doi.org/10.1007/s42452-019-0858-9
[6] Bahranowski, K., Klimek, A., & Gaweł, A. (2022). Rehydration-driven acid impregnation of thermally pretreated Ca-bentonite—Evolution of the clay structure. Materials, 15(6), 2018.
[7] Batros, S. S., Saeed, F. R., & Hussein, H. F. (2025). Antibacterial activity and microstructure properties of copper oxide particles doped with cadmium prepared by chemical precipitation method. Iranian Journal of Materials Science and Engineering, 22(1), 107–117. https://doi.org/10.22068/ijmse.3864
[8] Belousov, P. E., & Karelina, N. D. (2022). Volcano-sedimentary and hydrothermal bentonite deposits. Journal of Volcanology and Seismology, 16(6), 451–461.
[9] Boruah, J. S., & Chowdhury, D. (2023). Advances in carbon nanomaterial–clay nanocomposites for diverse applications. Minerals, 13(1), 1–14.
[10] Farhan, A. M., Zaghair, A. M., & Abdullah, H. I. (2022). Adsorption study of Rhodamine-B dye on plant (Citrus leaves). Baghdad Science Journal, 19(4), 838–847.
[11] Gola, A., Bernardi, A., & Pasut, G. (2021). The influence of initiator concentration on selected properties of thermosensitive poly(acrylamide-co-2-acrylamido-2-methyl-1-propanesulfonic acid) microparticles. Polymers, 13(7), 1–27.
[12] Hussein, H. F., Druga, L., Cojocaru, M., Dumitru, C., & Ghinea, A. (2018). Predicting and monitoring eutectic carbides proportion in cast austenitic Cr-Ni stainless steels. U.P.B. Scientific Bulletin, Series B: Chemistry and Materials Science, 80(4), 169–180. https://www.scientificbulletin.upb.ro/rev_docs_arhiva/full4c6_747566.pdf
[13] Hussein, H. F., Druga, L., Cojocaru, M., Dumitru, C., & Ghinea, A. (2020). The structural evolution of refractory steel spare parts during successive carburizing. U.P.B. Scientific Bulletin, Series B: Chemistry and Materials Science, 82(1), 247–257. https://www.scientificbulletin.upb.ro/rev_docs_arhiva/full715_295781.pdf
[14] Hasoon I.A., Inad K.I., Mahdi E.J., et al. (2025). Design and Performance Evaluation of an Off-Grid Photovoltaic System for Metallurgical Laboratories. JOM. https://doi.org/10.1007/s11837-025-07867-1.
[15] Jasim, B. E., Husain, A., & Aboud, N. (2022). Aqueous solution decolorization utilizing low-cost activated carbon produced from agricultural waste. Egyptian Journal of Chemistry, 65(SI), 1395–1400.
[16] Kamil, A. F., Abdullah, H. I., & Rheima, A. M. (2021). Cibacron red dye removal in aqueous solution using synthesized $CuNiFe_2O_5$ nanocomposite: Thermodynamic and kinetic studies. Egyptian Journal of Chemistry, 64(11), 6133–6145.
[17] Lima, E. C., Gomes, A. A., & Tran, H. N. (2020). Comparison of the nonlinear and linear forms of the Van't Hoff equation for calculation of adsorption thermodynamic parameters. Journal of Molecular Liquids, 311, 113315. https://doi.org/10.1016/j.molliq.2020.113315
[18] Mahdi, E. J., Hussein, H. F., & Saeed, F. R. (2025). Thermal performance comparison of aluminum and iron alloys in heat exchangers for solar water heating systems: Experimental study under Iraqi climate conditions. Next Materials, 8, 100935. https://doi.org/10.1016/j.nxmate.2025.100935
[19] Obaid, A.H., Mahdi, E.J., Hassoon, I.A., Hussein, F. H., Jasime, A.A.A.-S., Jafarf, A.N., & Abdulghanig, A.S. (2024). Evaluation of degradation factor effect on solar panels

performance after eight years of life operation. Archives of Thermodynamics, 45(3), 221–226. https://doi.org/10.24425/ather.2024.151223

[20] Pal, A., Majumder, K., Sengupta, S., Das, T., & Bandyopadhyay, A. (2017). Adsorption of soluble Pb(II) by a photocrosslinked polysaccharide hybrid: A swelling-adsorption correlation study. Carbohydrate Polymers, 177, 144–155. https://doi.org/10.1016/j.carbpol.2017.08.122

[21] Jaleel Mahdi,E. , Hussein,H. Fawzi, Azeez Hassoon,I. and Abd-Alsahb Jasim,A. (2025). Analysis of Solar Panel Surface Thermal Distribution Using Thermal Imaging. Journal of Renewable Energy and Environment, 12(4), 74-80. doi: 10.30501/jree.2025.495645.2207.

[22] Rheima, A. M., Mohammed, M. A., & Jaber, S. H. (2020). Adsorption of selenium (Se^{4+}) ions pollution by pure rutile titanium dioxide nanosheets electrochemically synthesized. Desalination and Water Treatment, 194, 187–193.

[23] Shaalan, B.A., Amer, N.A., Firas, H.K., Hussein, F. H., & Maha, S. N. (2024). Adsorption of phenol from aqueous solution using graphene nanoparticles. AIP Conference Proceedings, 3105, 070003. https://doi.org/10.1063/5.0212296

[24] Wang, J., & Guo, X. (2020). Adsorption isotherm models: Classification, physical meaning, application and solving method. Chemosphere, 258, 127279. https://doi.org/10.1016/j.chemosphere.2020.127279

[25] Zhang, T., Wang, W., & Zhao, Y. (2021). Removal of heavy metals and dyes by clay-based adsorbents: From natural clays to 1D and 2D nano-composites. Chemical Engineering Journal, 420, 127574. https://doi.org/10.1016/j.cej.2020.127574

[26] Saeed, F., Abdulkader, J. & Hussein, H. (2025). Advance analysis of aluminum alloy welded joints microstructure. Discover Materials. https://doi.org/10.1007/s43939-025-00491-5